

# Thetis benchmark Results

Stéphane Abadie and Lucie Clous

Laboratoire SIAME, UNIV PAU & PAYS ADOUR, EA4581, Anglet, France

## Abstract

A Navier-Stokes VOF model (THETIS) is tested against three benchmarks involving 3D block sliding and 2D granular submarine and subaerial slides. Simulations are compared with experiments giving slide motions as well as generated wave train features. Newtonian as well as  $\mu(I)$  rheology were used to simulate the slide motion. The results obtained in this exercise are detailed throughout the paper and more synthetically in the conclusions.

## 1 Model background

THETIS is a numerical simulation tool developed by University of Bordeaux. It is a versatile code to solve different problems: fluid flows, heat transfers, scalar transports or porous mediums. The potential of the code in the field of fluid flow is relatively large, it allows to solve incompressible or slightly compressible problems (laminar flow or turbulent flow), as well as multi-phase problems. It has also been validated and further developed in numerous studies related to water waves (Abadie et al., 1998; Lubin et al., 2006; Abadie et al., 2010; Mokrani and Abadie, 2016; Ducassou et al., 2017).

## 2 Model equations

In this benchmark study, the system of equations, also called one-fluid model, is composed of the incompressible Navier-Stokes equations (NS) and an additional equation for the interface evolution :

$$\left\{ \begin{array}{l} \nabla \cdot \mathbf{u} = 0 \\ \rho \left( \frac{\partial \mathbf{u}}{\partial t} + (\mathbf{u} \cdot \nabla) \mathbf{u} \right) = \\ \rho \mathbf{g} - \nabla p + \nabla \cdot [\eta (\nabla \mathbf{u} + \nabla^t \mathbf{u})] \end{array} \right. \quad (1)$$

$$\frac{\partial \chi}{\partial t} + \mathbf{u} \cdot \nabla \chi = 0 \quad (2)$$

In which,  $\rho$  and  $\eta$ , respectively density and viscosity of the fluid, are spatially varying variables and  $\chi(x, y, t)$  is a phase characteristic function equal to 1 in water and 0 in air.

## 3 Available rheology models

Three different rheology models may be used in THETIS:

1. the classical Newtonian fluid
2. the Bingham fluid
3. the  $\mu(I)$ -rheology

As a first approximation, landslide may be considered as a Newtonian fluid for which the viscosity value has to be tuned with respect to experimental data.

To be closer to the discontinuous media behavior, non-Newtonian fluid can be used. The formulation programmed here is the one used by Staron et al. (2013) in the code Gerris. The dynamic viscosity  $\eta$  is implemented as follows:

$$\eta_{Bingham} = \min\left(\frac{\tau_y}{D_2}; \eta_{max}\right) \quad (3)$$

The  $\mu(I)$ -rheology has also been implemented in Thetis. The latter has the form described by Lagr e et al. (2011) and implemented in Gerris, another Navier-Stokes code. The dynamic viscosity  $\eta$ , the friction coefficient  $\mu(I)$  and the inertial coefficient  $I$  are defined as follows:

$$\eta = \max\left(\frac{\mu(I)}{\sqrt{2}D_2} p, 0\right) \quad (4)$$

$$\mu(I) = \mu_s + \frac{\Delta\mu}{I_0/I + 1} \quad (5)$$

$$I = \frac{d\sqrt{2}D_2}{\sqrt{|p|/\rho}} \quad (6)$$

with  $D_2$  the second invariant of the strain rate tensor,  $p$  the pressure,  $\mu_s$ ,  $\Delta\mu$  and  $I_0$  three material-dependent coefficients,  $d$  the diameter of the grain and  $\rho$  the density of the grain.

This rheology has been initially developed for dry granular flow. In the case of granular flow in a viscous fluid, Cassar et al. (2005) have distinguished different regimes and adapted the expression of the inertial coefficient depending on the regime. This latter law is also implemented in THETIS.

## 4 Numerical method

### 4.1 Velocity and pressure solving

The NS equations are discretized on a fixed Cartesian grid using a finite volume formulation. Following (Patankar, 1990), the finite volumes formulation is solved using staggered mesh known as the Marker And Cells (MAC) method from (Harlow and Welch, 1965). For this reason, in THETIS the mesh is composed of two grids: the pressure grid and the velocity grid. The coupling between velocity and pressure can be solved using either the augmented Lagrangian method or the projection method. The first method is a very robust algorithm lying on an iterative procedure which may in some case be quite costly. The latter is an accurate and fast procedure to obtain divergence free velocity field but may fail in particular boundary condition cases.

#### 4.1.1 Augmented Lagrangian method

This is a minimization method under the constraint of the continuity equation, where the pressure, which is decoupled from the velocity, appears as a Lagrange multiplier. The incompressibility constraint is directly introduced into the equation of motion as a penalty term  $r_u \nabla(\nabla \cdot \mathbf{v})$ , which couples the velocity components. At each time step  $n$  and at iteration  $k$ , the system is written as:

$$\rho^n \left( \frac{\mathbf{v}^{n,k+1}}{\Delta t^n} + (\mathbf{v}^{n,k} \nabla) \mathbf{v}^{n,k+1} \right) - \rho^n \mathbf{b} - \nabla p^{n,k} - \nabla [r^n (\nabla \mathbf{v}^{n,k+1} + \nabla^t \mathbf{v}^{n,k+1})] - r_u \nabla(\nabla \cdot \mathbf{v}^{n,k+1}) = \rho^n \frac{\mathbf{v}^n}{\Delta t^n} \quad (7)$$

$$p^{n,k+1} = p^{n,k} - r_p \nabla \cdot \mathbf{v}^{n,k+1}, \quad (8)$$

where  $r_u$  and  $r_p$  are convergence parameters. The advantage of such a formulation is the explicit calculation of the pressure. It uses only the pressure in the previous temporal iteration and the divergence of velocity.

### 4.1.2 Projection method

This method comprises two steps:

1. from the pair  $(u^n, p^n)$ , a velocity field  $\tilde{u}$  is calculated using the expression :

$$\tilde{u} - u^n = \frac{\Delta t^n}{\rho^n} (\rho^n g - \nabla p^n + \nabla(\eta^n(\nabla u^n + \nabla^t u^n)) - \nabla \cdot (\rho^n u^n \otimes u^n)) \quad (9)$$

2. The velocity  $u$  is calculated by projection of  $\tilde{u}$  on a field with no divergence

$$u^{n+1} = \tilde{u} - \frac{\Delta t^n}{\rho^n} \nabla(p^{n+1} - p^n) \quad (10)$$

This second step (projection step) involves determining the pressure  $p^{n+1}$ . We use the Poisson equation:

$$\nabla \left( \frac{\Delta t^n}{\rho^n} \nabla(p^{n+1} - p^n) \right) = \nabla \tilde{u} \quad (11)$$

This method is relatively simple to program and easy to solve because it is not an iterative method (contrary to the previous method). However, the boundary conditions on the pressure must be imposed to allow the resolution of (11).

## 4.2 Interface tracking

Equation (2) is solved by introducing a color function  $F$  defined as the average of the phase characteristic function  $\chi(x, y, z)$  over the mesh cell. With this definition,  $F$  indicates the volume fraction occupied by water in a mesh cell and the interface position is defined as the iso-line  $F = 0.5$ .

At the end of each time step, the local cell water volume fraction is used to recalculate local values of density and viscosity necessary to solve the NS equations. For cells containing a fraction of water and air, equivalent density and viscosity are calculated by interpolations (linear for density and harmonic for viscosity) based on the water fraction. Different VOF methods are implemented in the model THETIS to solve equation (2).

## 4.3 VOF-TVD method

This first method consists in solving equation (2) directly using a suitable numerical scheme. Writing the convective term of equation (2) in the conservative form and using a first order discretization in time, the discretization in space over the volume control  $(i, j)$  reads :

$$\frac{F_{i,j}^{n+1} - F_{i,j}^n}{\Delta t^n} \Delta X \Delta Y + \Phi_X \Delta Y + \Phi_Y \Delta X = 0 \quad (12)$$

with :

$$\Phi_X = F_{i+\frac{1}{2},j}^{n+1} u_{i+1,j}^{n+1} - F_{i-\frac{1}{2},j}^{n+1} u_{i,j}^{n+1} \quad (13)$$

$$\Phi_Y = F_{i,j+\frac{1}{2}}^{n+1} u_{i,j+1}^{n+1} - F_{i,j-\frac{1}{2}}^{n+1} u_{i,j}^{n+1} \quad (14)$$

$\Delta X$  (respectively  $\Delta Y$ ) represents the horizontal space step (respectively vertical). At this stage, a good approximation of the fluxes  $\Phi_X$  and  $\Phi_Y$  is required to obtain an accurate representation of the interface. A TVD scheme typically has two main properties : in the parts of the domain where the solutions are regular, it is equivalent to a high-order scheme that reduces diffusion, and in the parts where there are strong discontinuities it is a first order scheme that prevents oscillations.

#### 4.4 VOF-PLIC method

The Piecewise Linear Interface Calculation (PLIC) method is also employed (Youngs, 1982). One of the great advantage of this Eulerian/Lagrangian method is to keep the discontinuous nature of the interface between water and air thanks to the Lagrangian character of the transport method. The five successive steps of the PLIC method are the followings:

- Mixed cells (i.e.  $0 < F < 1$ ) identification.
- In each cell containing air and water, calculation of the interface normal direction using a finite difference approximation on nine points.
- Piecewise linear interface reconstruction, knowing the normal direction in each cell and the volume fraction.
- Lagrangian advection of the interface segments using a linear interpolation of velocities calculated on the staggered mesh.
- Calculation of the new volume fraction distribution.

To ensure the conservative or stability nature of the PLIC method, a sufficient condition is that the segments are not advected over more than half of a cell size during a time step (Abadie et al., 1998).

#### 4.5 SVOF-PLIC method

The SVOF-PLIC method, used in complement of PLIC, consists in slightly smoothing the volume fraction function by introducing a controlled diffusion zone around the interface. This is performed by using an analogy with the thermal diffusion whose governing equation equation reads:

$$\frac{\partial T}{\partial t} - \nabla \cdot (a \nabla T) = 0 \quad (15)$$

$a > 0$  being the thermal diffusivity coefficient. The smoothed volume fraction function  $F^S$  is built from equation (15) discretized in time :

$$-\nabla \cdot a \nabla F^{S,n+1} + F^{S,n+1} = F^{S,n} \quad (16)$$

In which the equivalent diffusion coefficient  $a$  is related to the interface thickness  $L_i$  and the local dimension of the considered cell  $\Delta X$  by :

$$a = L_i \Delta X^2 \quad (17)$$

Equation (17) is discretized in space using the finite volume method and a centered scheme. The final smoothed function  $F^S$  is obtained iteratively by applying the following algorithm :

$$L^1 = F \quad (18)$$

$$\text{For } k = 1 \dots N - 1, \text{ solve} \quad (19)$$

$$-\nabla \cdot \tau_d^* \nabla F^{S,k+1} + F^{S,k+1} = L^k \quad (20)$$

$$L^{k+1} = F^{S,k+1} \quad (21)$$

with  $\tau_d^*$  defined by  $\tau_d^* = L_i \Delta h^2 / N$ . After resolution of (18) - (21), the condition  $F^S = F^{S,N}$  is verified.

The function  $F^S$  includes a narrow diffusion zone that represents the interface more regularly. By this way, the discontinuities which may appear with the PLIC algorithm are smeared and the interface is more stable while being a little less accurate. The model can then describe high interface distortions. Practically, the parameters and the number of internal iterations are adjusted to limit the interface fractioning while keeping an accurate description of the interface.

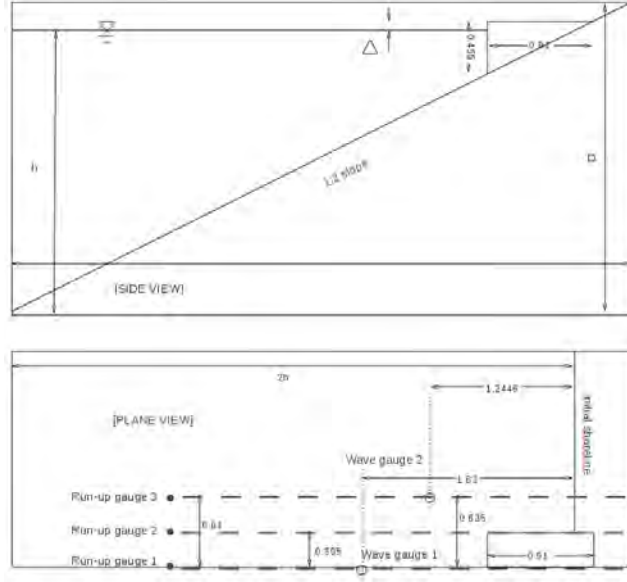


Figure 1: Sketch of Benchmark 3

## 5 Benchmark problem comparison

### 5.1 Benchmark 3: 3D - Subaerial and Submarine solid slide with rectangular plan and vertical sides (Liu et al., 2005)

In benchmark 3 (Figure 1), augmented Lagrangian and PLIC VOF methods are used. Instead of prescribing slide motion (like in (Liu et al., 2005) for instance), we solved for the full coupling between slide and water and hence calculated slide motion as part of the solution, where the rigid wedge is modeled as a Newtonian fluid of large viscosity ( $10^5 Pa.s$ ). Here, we present in detail the first benchmark case in which the slide initial submergence is  $\Delta = -0.1m$  and slide density ratio is 2.14;  $x'$  is in the slope direction,  $z'$  is perpendicular to the slope plane (gravity being in this case inclined by  $26.56^\circ$  with respect to  $z'$ ),  $y = y'$  is in the longshore direction. Due to symmetry with respect to the middle vertical plane, the computational domain only represents half the experimental flume (including run-up gage 1 and wave gage 1). Two numerical grids were tested to assess discretization effects on slide motion and, subsequently, on free surface deformation. Both grids were irregularly distributed over  $x'$  and  $z'$  to account for the need for finer resolution close to the generation zone. The first grid (mesh 1, with  $62 \times 76 \times 24$  cells) is comparable to the mesh used in (Liu et al., 2005). The finest grid cell size is  $\Delta x' = 0.039$  m,  $\Delta z' = 0.0196$  m,  $\Delta y'$  being constant and equal to 0.077 m. For the second mesh used (mesh 2, with  $170 \times 100 \times 120$  cells), the finest grid cell size is  $\Delta x' = \Delta z' = 0.015$  m,  $\Delta y'$  was constant and also equal to 0.015 m. The nondimensional finest grid sizes are respectively  $\Delta x'/L = \Delta z'/L = 3.8\%$  for mesh 1 and 1.4% for mesh 2 (with  $L = 1.017$  m). High resolution 3D computations are very computationally intensive and therefore simulations were run using the parallel version of our model.

Figure 2 shows snapshots of water/air and slide/water interfaces computed at four different times steps for the finest mesh, using the NS-PLIC model. In the last image at  $t = 3.5$  s, the slide has stopped on the horizontal bottom of the experimental flume, which is represented in simulations but not visible on Fig. 3. In this snapshot sequence, we observe the generation of a wave train, and its subsequent propagation and reflection from the vertical sidewalls of the flume. Maximum run-up, which occurs at the plan of symmetry on the flume axis, is seen to also propagate towards and reflect of the sidewalls.

Figure 3 shows the simulated slide of mass motion as a function of time, as compared to experimental data. The measured slide motion is well reproduced in the finer mesh grid, with a RMS deviation of 0.16 m. In the coarser grid, the slide is much slower than in experiments (larger RMS deviation of 0.80 m).

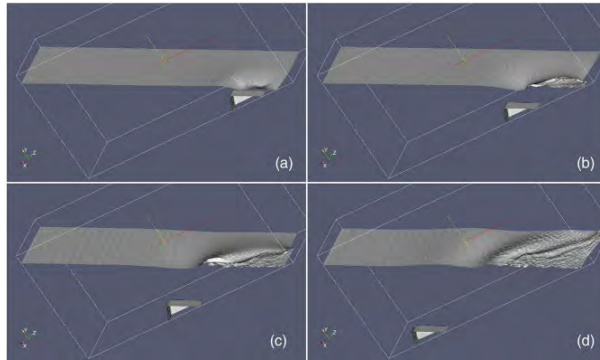


Figure 2: Snapshots of slide/water and water/air interfaces at different times for grid 2 with 170x100x120 cells. Slide initial submergence is  $\Delta = -0.1$  m, slide density is 2.14. (a)  $t=0.7$ s, (b)  $t=1.4$ s, (c)  $t=2.1$ s, (d)  $t=3.5$ s.

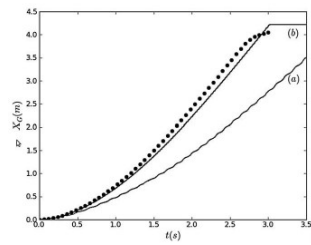


Figure 3: Case of Figure 2. Time evolution of slide center of mass . Solid lines : numerical results with (a) 62x76x24 cells and (b) 170x100x120 cells; ( $\star$ ): experimental data. Initial slide submergence is  $\Delta = -0.1$ m, slide density is 2.14.

A computation performed using an intermediate grid size (not presented here) yielded a slide motion curve in between the two presented curves, indicating a consistent of the model. Other computations for different initial submergence values also matched experimental data well, provided that a fine enough grid (i.e., with  $\Delta x/L \approx 1\%$ ) is used. A closer inspection of our results indicates that, resolving the coupling between slide motion and water flow in the numerical model is achievable with good accuracy, but requires an overall grid about 20 times larger than when slide motion is a priori specified, as in Liu et al. (2005).

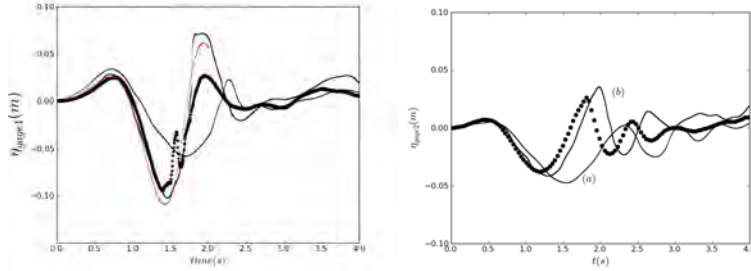


Figure 4: Case of Fig. 3. Comparison between numerical results (solid lines) and experimental data ( $\star$ ) for the time histories of free surface elevations at wave gage 1 (Fig. 5 top) and wave gage 2 (Fig 18b). Initial slide submergence is  $\Delta = -0.1\text{m}$ , slide density is 2.14. (a) 62x76x24 cells, (b) 170x100x120 cells, and 260x200x120 : red curve Fig. 5 top.

Figure 4 compares surface elevations simulated at wave gages 1 and 2, both in the generation area, to experimental data. At gage 1, both the first elevation wave and through are well modeled in the finer grid 2 (respectively 17% and 5% of relative errors), whereas the second wave is much higher (162%) than measured. Our last attempt using a finer grid step (mesh : 260x200x120) helps reducing the error from 162% to 114% for this second wave. Both wave phase and hence celerity, however, are correctly predicted in the finer grid 2, whereas the second wave is too slow in the coarser grid 1. Note that wave heights are also under-predicted in the latter grid, which is consistent with a slower slide. At gage 2, the lateral spreading of the wave is also well simulated using grid 2; the simulated wave elevations are close to the experimental results (17%, 10%, 30% respectively for wave crest 1, through 1, wave crest 2), even though waves seem to be a bit slower. In grid 1 again, the slower slide generates both smaller and slower waves as compared to experimental data.

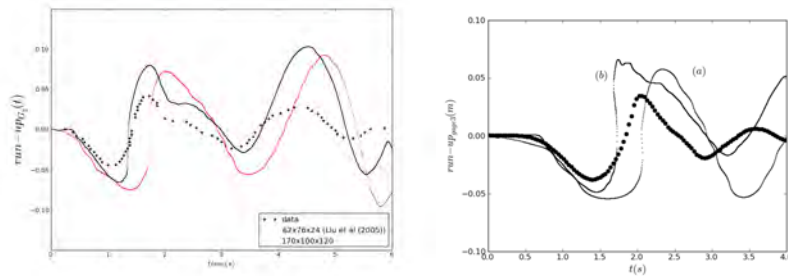


Figure 5: Case of Fig. 3. Comparison between numerical results (solid lines) and experimental data ( $\star$ ) for the time histories of run-up at (left) gage 2 and (right) gage 3 (Figure 1). Initial submergence is  $\Delta = -0.1\text{m}$ , slide density is 2.14. (a) 62x76x24 cells, (b) 170x100x120 cells

Figure 5, similarly, compares run-up simulated at run-up gages 2 and 3 (see Figure 1) to experimental data. At gage 2, in the finer grid, numerical results closely match experiments, except during the first

run-up phase where the model overestimates the recorded run-up value and generates a quicker run-up motion. In the coarser grid, run-down and run-up values are both overestimated. A similar behavior is observed at gage 3. Note that we used here a free slip boundary condition on the bottom, which may explain the overestimation of the run-up results. The model accuracy may be improved by using a no-slip condition.

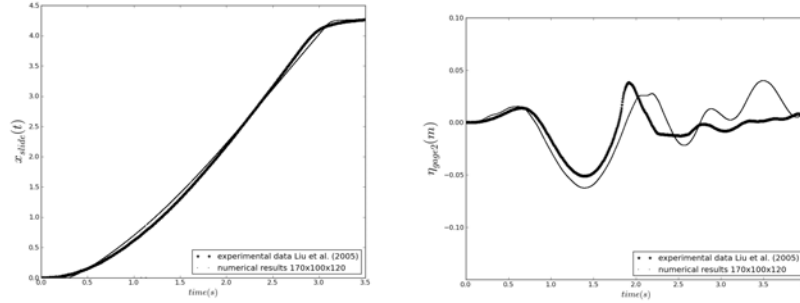


Figure 6: Case 2 :  $\Delta = -0.025m$ . left : Time evolution of slide center of mass. Solid line : numerical results with 170x100x120 cells ; ( $\star$ ): experimental data, right : time histories of free surface elevations at wave gage 2

Finally, we also simulated the second benchmark case featuring the same rigid body, but with a lower submergence  $\Delta = -0.25m$  and a higher slide density ratio of 2.79. In the finer mesh, whose corresponding results are only shown here, slide motion is accurately predicted (Figure 6 left panel). Also a comparison of free surface elevation at wave gage 2, presented on Figure 6 right panel, shows the accuracy that may be expected by using THETIS in this kind of problems.

## 5.2 Benchmark 4: 2D - Deformable submarine slide (Grilli et al., 2017)

The experiment in the benchmark 4 consists in releasing a volume of glass beads underwater on a slope. The flume sketch is presented on Figure 7. The numerical domain has a length of 6.27 m and 0.33 m of water height. The resolution in the zone of interest is  $\Delta x = 0.00285 m$  and  $\Delta y = 0.00125 m$ . The flow is solved using the projection method and the TVD VOF scheme. The slide is modeled as a Newtonian fluid, first with parameters defined in Grilli et al., i.e. a viscosity of 0.01 Pa.s and a density of 1951 kg.m<sup>-3</sup>. A few other viscosity values were also tested to evaluate the sensitivity of the model. No simulation with the  $\mu(I)$ -rheology are presented as the flow initiation has been proved to be difficult with the usual parameters.

Results of the slide shape and wave heights are presented in Figures 8 and 9.

The slide shape evolution as well as the slide overall velocity is shown to strongly depend on the viscosity value. For the quite weak viscosity used in Grilli et al. (2017), the slide head exhibits a bulge head due to the presence of a strong counter-clockwise vortex generated at the water/slide interface. This vortex is weaker and weaker when increasing the viscosity value. The experimental snapshots also show the occurrence of this vortex more or less consistent with the results corresponding to the two stronger viscosities tested in our simulations. Nevertheless, in all the cases tested, the slide motion appears to be too slow compared to the experiment. The best approximation would be with the lowest viscosity but due to the aforementioned large vortex and the subsequent additional drag induced, velocity can finally not reach higher values. We have tried several strategies to produce faster slides such as vanishing the basal friction, etc. but they all turned out to fail. Our explanation is that the slide is simulated as an equivalent phase instead of a granular water mixed medium. The latter allows water to flow within (as a cage would for instance slide in water) whereas the former do not. This differential flow may reduce the global slide drag and explain the final velocity reached in the experiment.

Figure 9 shows that with a slide viscosity of 0.01 Pa.s, the first wave is higher than the experimental value and the wave train is not correctly reproduced on the first gauge. By reducing the viscosity, the generated waves are lower. We observe that with a viscosity of 1 Pa.s, the first wave is close to the

experimental results as well as the first waves in the train wave. Overall the results on wave height appears satisfactory for slide motions shown to be slower than in the experiment. This calls for further investigations.

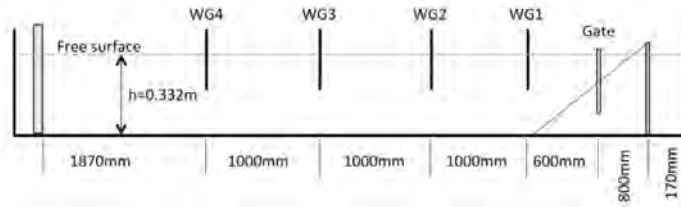


Figure 7: Sketch of Benchmark 4

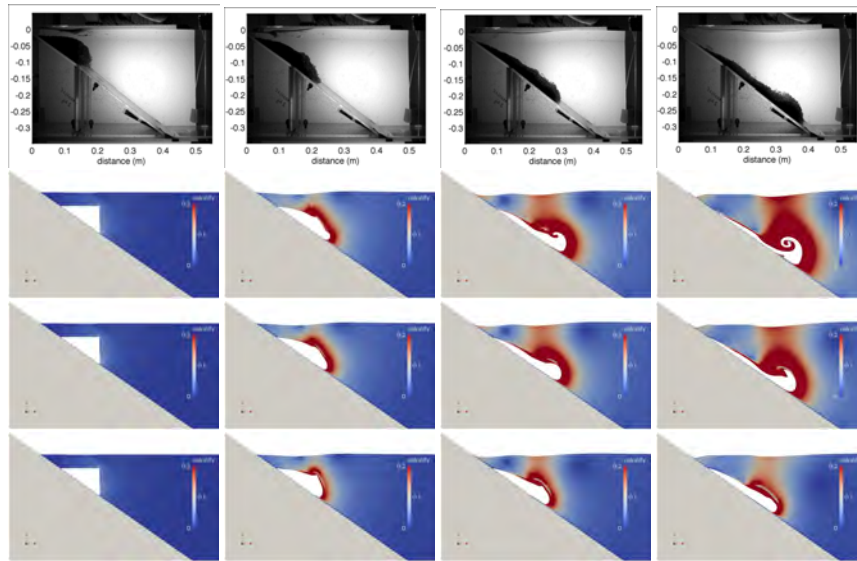


Figure 8: Comparison of the slide during the experiment (first row) and simulations for different values of viscosity ( $\eta = 0.01, 1, 10 Pa.s$  for second, third and fourth row respectively) at times  $t = 0.02, 0.17, 0.32, 0.47 s$

### 5.3 Benchmark 5: 2D - Deformable subaerial slide (Viroulet et al., 2014)

In benchmark 5, a volume of glass beads is released above water unlike the benchmark 4. The 2D experiment was carried out in a flume of dimensions  $2.20 m$  long,  $0.4 m$  high and  $0.2 m$  wide. The beads are placed on a  $45^\circ$  slope as in the Figure 10. Glass beads have a density of  $2500 kg.m^{-3}$  and a diameter of  $1.5 mm$  in the first case,  $10 mm$  in the second. Water depth is  $14.8 cm$  and  $15 cm$  for the first and second case respectively. 4 gauges monitor the surface elevation at  $x_1 = 0.45 m$ ,  $x_2 = 0.75 m$ ,  $x_3 = 1.05 m$  and  $x_4 = 1.35 m$ .

Numerically, the slide is modeled as a fluid with a Newtonian rheology. Simulations with a  $\mu(I)$ -rheology were also performed. The space and time steps are  $\Delta x = 5 mm$ ,  $\Delta y = 2 mm$  and  $\Delta t = 10^{-3} s$ . The flow is solved thanks to the projection algorithm and a VOF-TVD interface tracking is performed.

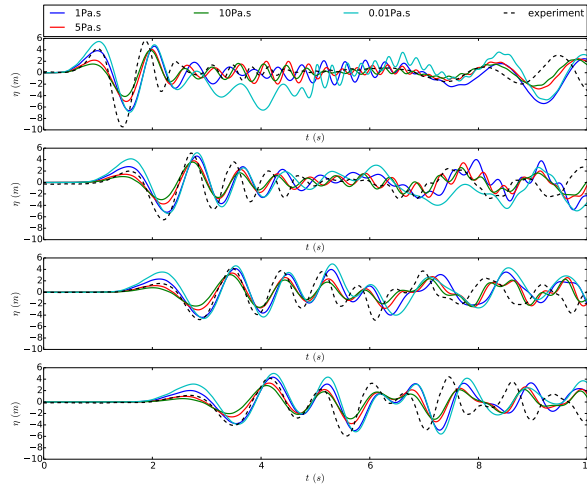


Figure 9: Elevation of the free surface, comparison between the experiment and the simulations with different viscosity values

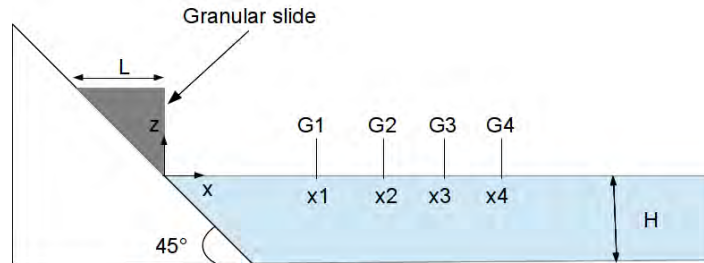


Figure 10: Sketch of Benchmark 5

For the first case, simulations with different values of viscosity were carried out. With low viscosity values, the slide is faster and a vortex is observed similarly to the experiment (Figure 11). The best results in terms of slide motion were obtained with a viscosity of  $2 Pa.s$ , even though in this case the slide is a bit slower than in the experiment.

However, if we now compare the height of the first wave at the four gauges (Figure 12), it appears to be almost twice as high as the experimental results for this viscosity. At lower viscosity, the free surface elevation seem to be discontinuous because it is more perturbed due to wave breaking and harder to capture at the gauges. The first wave and the wave train that follows is well reproduced for a viscosity of  $10 Pa.s$ , even if the slide at this viscosity is shown to be slower than in the experiment as in the previous benchmark. The same overall behaviour is observed in the second case with a glass beads diameter of  $10 mm$  (Figure 13), but a higher value of viscosity has to be set in order to fit the experimental wave heights.

The density of the slide which has to be taken into account in the simulation may be questioned. Indeed, at  $t = 0 s$ , the slide being at rest above water, with a random close pack, the maximum volume fraction of beads is about 60%, which gives a density of  $1500 kg.m^{-3}$  for the slide. Yet, during most of the experiment, the slide is into water, the maximum density for a random close pack is then  $1900 kg.m^{-3}$ . However, if we observe the slide, the beads do not form a close pack and its volume expands (almost a 50% expansion !), the latter density is maximal. Simulation were run with this density

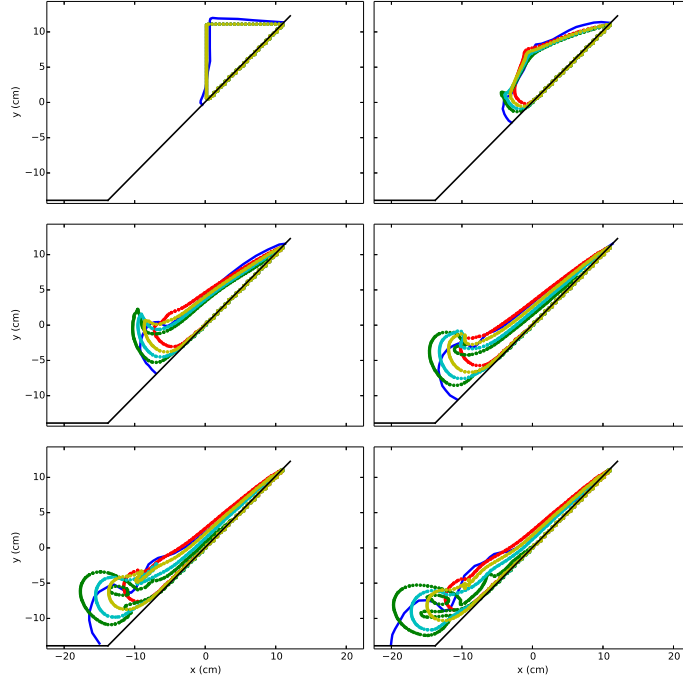


Figure 11: Contour of the slide during the experiment (blue line) and the simulations for different values of slide viscosity,  $\eta = 1 Pa.s$ : green points,  $\eta = 2 Pa.s$ : cyan points,  $\eta = 5 Pa.s$ : yellow points and  $\eta = 10 Pa.s$ : red points; 0.1 s between two figures

to show its influence on the wave heights (Figure 14). The change of density has little influence on the wave heights. First and second waves are only slightly higher with the  $1900 kg.m^{-3}$  density.

The first benchmark case was also simulated with the  $\mu(I)$ -rheology using parameters of the literature:  $\mu_s = 0.43$ ,  $\Delta\mu = 0.39$ ,  $I_0 = 0.27$ . Figure 15 shows the evolution of the viscosity inside the slide during the simulation. After entering water, the viscosity at the tip of the slide gets higher and the slide quickly stops. It seems that the water slows down the slide too much and as deformation decreases in the  $\mu(I)$  formulation, the viscosity increases and this behavior ends up stopping the slide. However, waves are generated very quickly in this experiment and we can see in Figure 17 that the wave height is quite close to the experimental results. Comparing to the computation with the Newtonian fluid, during the first 0.5 s where the waves are generated, the deformation of the slide is very similar to the Newtonian slide (Figure 16).

## 6 Conclusions

In this paper, Navier-Stokes VOF simulations (THETIS) were run on benchmarks 3,4 5, involving respectively, 3D solid block slide, submarine and subaerial granular slides. For benchmark 3, the results show that if the model is able to simulate the slide motion accurately, yet the coupling with the free surface is hard to capture in 3D. In benchmark 4, a Newtonian slide was simulated. The sensitivity on slide viscosity appears to be relatively weak for this case regarding the wave train. Whereas the influence on the slide shape is important. Tuning slide viscosity at best allows to reproduce the main features of the wave train while the slide is always too slow. Benchmark 5 is more complex with penetration in water and density and volume variations. The Newtonian model is shown to perform again pretty well in terms of wave heights but generated slides are still too slow. In this case, the sensitivity on slide viscosity is high in slide shape as well as in wave heights. Finally, the  $\mu(I)$  rheology was able to produce the right

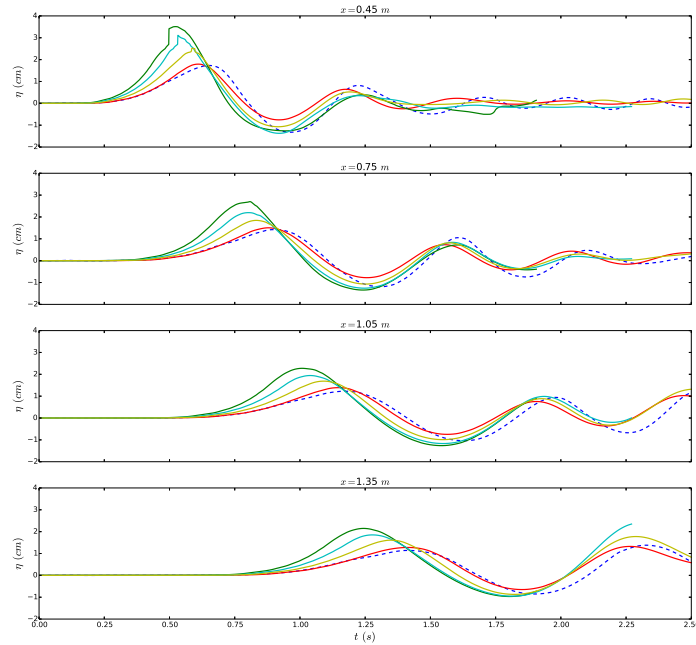


Figure 12: Elevation of the free surface at the gauges for the experiment (blue discontinuous line) and the simulations for different values of viscosity,  $\eta = 1 Pa.s$ : green line,  $\eta = 2 Pa.s$ : cyan line,  $\eta = 5 Pa.s$ : yellow line and  $\eta = 10 Pa.s$ : red line; 0.1 s between two figures

wave train without any a priori calibration.

## 7 Acknowledgments

The authors acknowledge financial support for this work from the PIA RSNR French program TANDEM (Grant No.: ANR-11-RSNR-00023-01). LC's PhD grant is funded by Univ. Pau and Pays Adour. The authors thanks the organizers of this workshop for inviting them to participate to this benchmark exercise.

## References

- Abadie, S., Caltagirone, J., and Watremez, P. (1998). Splash-up generation in a plunging breaker. *C.R.A.S. - mechanics, Serie II*:553–559.
- Abadie, S., Morichon, D., Grilli, S., and Glockner, S. (2010). Numerical simulation of waves generated by landslides using a multiple-fluid navier–stokes model. *Coastal engineering*, 57(9):779–794.
- Cassar, C., Nicolas, M., and Pouliquen, O. (2005). Submarine granular flows down inclined planes. *Physics of fluids*, 17(10):103301.
- Ducassou, B., Nuñez, J., Cruchaga, M., and Abadie, S. (2017). A fictitious domain approach based on a viscosity penalty method to simulate wave/structure interaction. *Journal of Hydraulic Research*, pages 1–16.

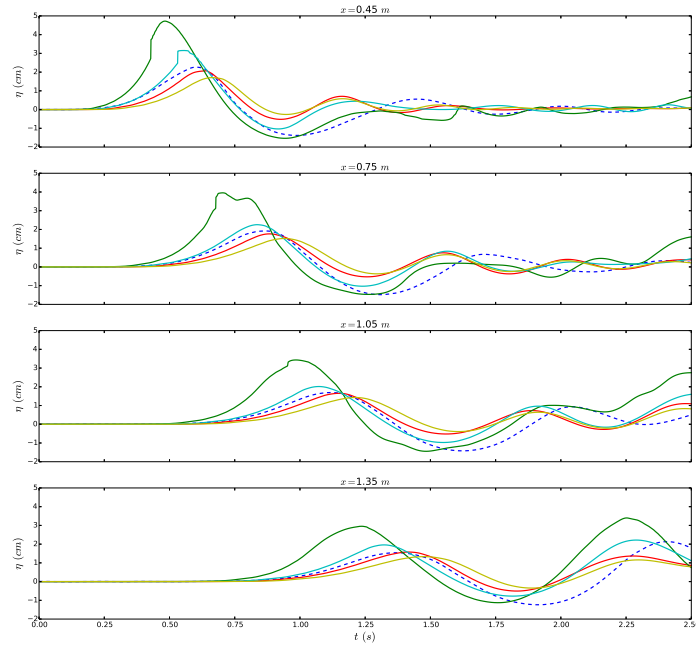


Figure 13: Elevation of the free surface at the gauges for the experiment (blue discontinuous line) and the simulations for different values of viscosity,  $\eta = 0.2 Pa.s$ : green line,  $\eta = 10 Pa.s$ : cyan line,  $\eta = 20 Pa.s$ : red line and  $\eta = 30 Pa.s$ : yellow line; 0.1 s between two figures

- Grilli, S. T., Shelby, M., Kimmoun, O., Dupont, G., Nicolsky, D., Ma, G., Kirby, J. T., and Shi, F. (2017). Modeling coastal tsunami hazard from submarine mass failures: effect of slide rheology, experimental validation, and case studies off the us east coast. *Natural hazards*, 86(1):353–391.
- Harlow, F. H. and Welch, J. E. (1965). Numerical calculation of time-dependent viscous incompressible flow of fluid with free surface. *The physics of fluids*, 8(12):2182–2189.
- Lagrée, P.-Y., Staron, L., and Popinet, S. (2011). The granular column collapse as a continuum: validity of a two-dimensional navier–stokes model with a  $\mu$  (i)-rheology. *Journal of Fluid Mechanics*, 686:378–408.
- Liu, P.-F., Wu, T.-R., Raichlen, F., Synolakis, C., and Borrero, J. (2005). Runup and rundown generated by three-dimensional sliding masses. *Journal of fluid Mechanics*, 536:107–144.
- Lubin, P., Vincent, S., Abadie, S., and Caltagirone, J. (2006). Three dimensional large eddy simulation of air entrainment under plunging breaking waves. *Coastal engineering*, 53:631–655.
- Mokrani, C. and Abadie, S. (2016). Conditions for peak pressure stability in vof simulations of dam break flow impact. *Journal of Fluids and Structures*, 62:86–103.
- Patankar, S. (1990). Numerical heat transfert and fluid flow. *Hemisphere publishing Corporation, New york*.
- Staron, L., Lagrée, P.-Y., Ray, P., and Popinet, S. (2013). Scaling laws for the slumping of a bingham plastic fluid. *Journal of Rheology*, 57(4):1265–1280.

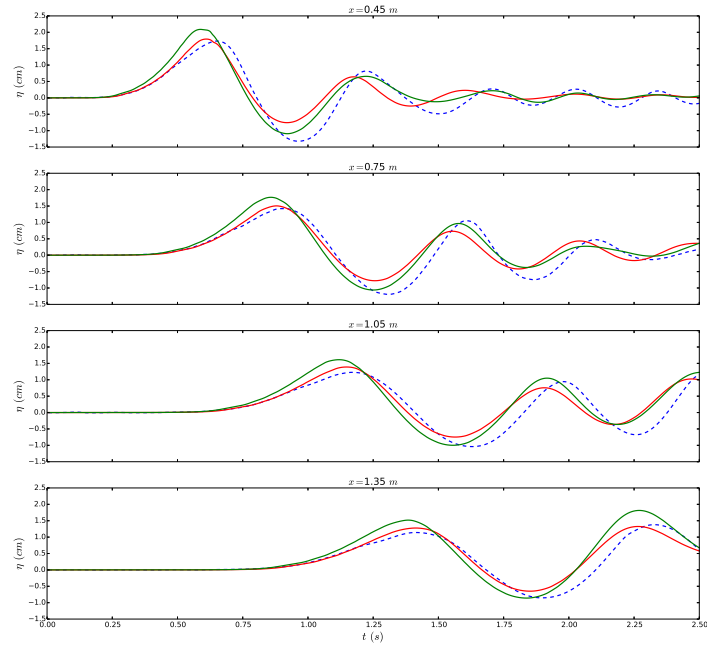


Figure 14: Elevation of the free surface at the gauges for the experiment (blue discontinuous line) and the simulations for two values of density,  $\rho = 1900 \text{ kg.m}^{-3}$ : green line and  $\rho = 1500 \text{ kg.m}^{-3}$ : red line

Viroulet, S., Sauret, A., and Kimmoun, O. (2014). Tsunami generated by a granular collapse down a rough inclined plane. *EPL (Europhysics Letters)*, 105(3):34004.

Youngs, D. (1982). *Numerical methods for fluid dynamics*. New York American Press.

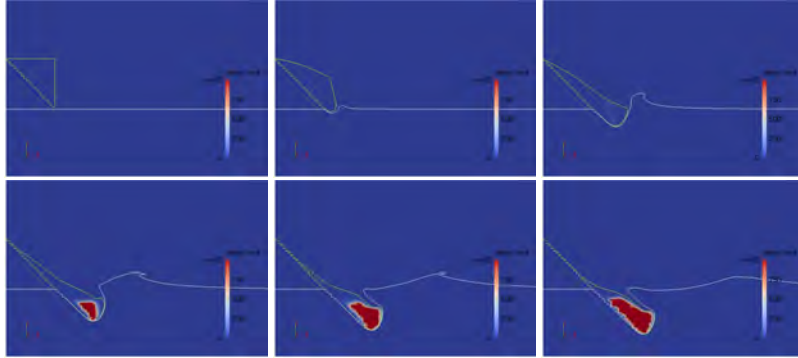


Figure 15: Evolution of the viscosity inside the slide, 0.1 s between two figures

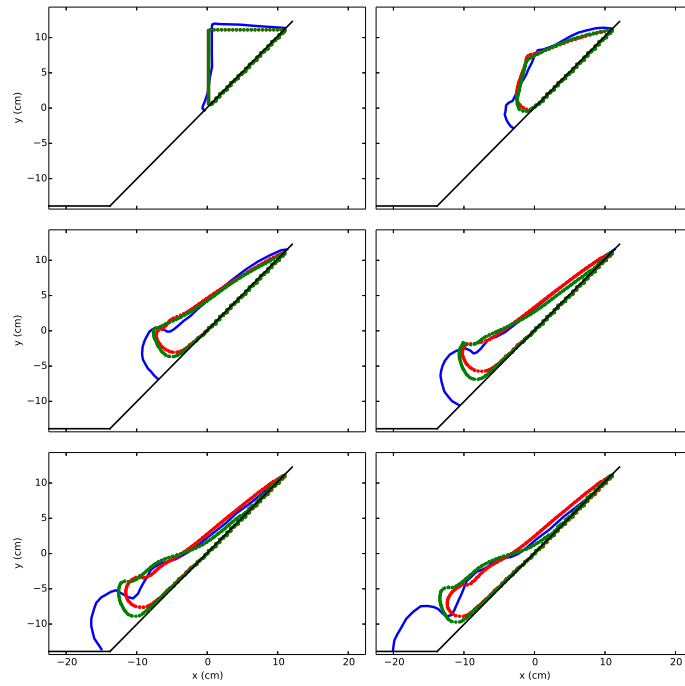


Figure 16: Contour of the slide during the experiment (blue line) and the simulations for a Newtonian fluid with  $\eta = 10 \text{ Pa}\cdot\text{s}$ : green points and the  $\mu(I)$ -rheology: red points; 0.1 s between two figures

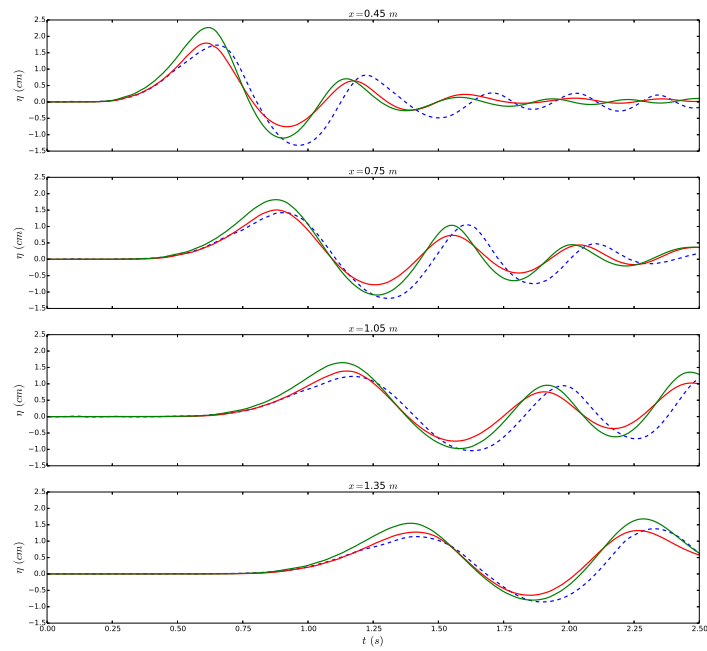


Figure 17: Elevation of the free surface at the gauges for the experiment (blue discontinuous line) and the simulations for a Newtonian fluid with  $\eta = 10 \text{ Pa}\cdot\text{s}$ : green points and the  $\mu(I)$ -rheology: red points